

The effects of curing temperature on bilayer and monolayer hybrid films: mechanical and electrochemical properties

S. R. Kunst · H. R. P. Cardoso · M. R. Ortega V ·
L. V. R. Beltrami · T. L. Menezes · C. F. Malfatti

Received: 31 January 2014 / Accepted: 19 May 2014 / Published online: 6 June 2014
© Springer Science+Business Media Dordrecht 2014

Abstract Thermal curing contributes to the formation and performance of hybrid films (HFs), because it enhances barrier properties by reticular densification, which originates from a less porous layer, and improves corrosion protection and mechanical properties. Increasing the number of deposited layers further enhances these properties. In this work, a HF formed by an alkoxide precursor solution of 3-(trimethoxysilylpropyl) methacrylate and tetraethoxysilane with cerium nitrate and polyethylene glycol was applied to the galvanized steel. The films were obtained by either monolayer or bilayer dip coating, and they were cured at different temperatures (60 and 90 °C) for 20 min. The results indicate that both the temperature and the number of layers interfere on the ability of HFs to act as effective barriers against corrosion. The bilayer system cured at 60 °C showed the best electrochemical impedance results; however, the monolayer HF cured at 90 °C presented higher wear resistance.

Keywords Hybrid film · Temperature · Bilayer · Corrosion · Galvanized steel

1 Introduction

Hybrid films (HFs) obtained using the sol–gel method are not effective barriers to corrosion; thick films are not

sufficient because they may contain defects. To increase barrier protection, plasticizers, such as poly(methyl methacrylate) [1] or polyethylene glycol, PEG [2], have been used to increase coating thickness and sol viscosity, and to improve the flexibility of the system to obtain uncracked films that can be subjected to mechanical deformation without failure [3].

Generally, siloxane–PEG HFs are homogeneous and present good chemical and thermal stability. Additionally, these coatings have excellent barrier properties that improve the corrosion protection of pretreated substrates. These films act primarily as a barrier-type layer between the substrate and the environment. Thus, they reduce the entry rate of water, electrolytes and oxygen and inhibit the permeation of species to the interface of the metal, which decreases the corrosion rate of the substrate. Accordingly, the degree of hydrophobicity and adhesion to the substrate (formation of strong covalent bonds; MeOSi) [1, 2] is important properties of these films.

HFs obtained by the sol–gel process have the advantage of being processed at low temperatures. For this reason, neither solvent volatilization nor degradation of chemical species is observed [4]. The development of novel silane HFs based on organic–inorganic pretreatments has partially solved the temperature problem because they can be cured at low temperatures, which preserves the integrity of the metallic substrate and diminishes crack formation. In this sense, coatings that can be cured at low temperatures are an attractive possibility for galvanized steel because they provide good corrosion resistance [5]. The coatings processed using the sol–gel method have been presented as potential substitutes for treatments based on chromium(VI), which are toxic and carcinogenic [6].

The sol–gel process is a simple method with low-cost installation that has been widely exploited for the preparation

S. R. Kunst (✉) · H. R. P. Cardoso · M. R. Ortega V ·
L. V. R. Beltrami · C. F. Malfatti
LAPEC, Federal University of Rio Grande do Sul – UFRGS,
Avenida Bento Gonçalves, Porto Alegre, RS 9500, Brazil
e-mail: tessaro.sandra@gmail.com

T. L. Menezes
LACOR, Federal University of Rio Grande do Sul – UFRGS,
Avenida Bento Gonçalves, Porto Alegre, RS 9500, Brazil

of thin films [7, 8]. After using appropriate techniques to deposit the film on the substrate, the film is exposed to air, which initiates hydrolysis and condensation reactions. After drying for a few minutes, a hybrid (organic and inorganic) network (gel) is formed on the substrate [9, 10].

By sintering (densification) at an appropriate temperature, the organic groups and water molecules are eliminated and oxides (OXs) are formed. The film is then subjected to a final heat treatment to control the desired structure [11]. However, temperature variations affect the hydrolysis and condensation reactions during the formation of HFs [12]. Thicker films improve the effectiveness of the barrier against corrosion and may be obtained by increasing the number of layers [13].

The thickness of the coupling agent layer is an important factor in adhesion. The thick siloxane layer may contain chemically and physically absorbed layers with weak interfaces that can decrease the adhesive strength. Thicker films can also become brittle [14]. However, the optimum thickness value depends on the bonded materials [15]. The substrate surface also affects the formation of HF layers. A rough surface may disrupt the order of the first HF layer, which prevents the formation of the second layer. Thus, smooth surfaces are the best substrates for silane bonding [16]. Studies [1, 2] have shown that one silane layer is not enough to provide suitable corrosion protection to metallic substrates. Therefore, bilayer coatings are recommended, which suggests the application of a two-step treatment.

The study by Malfatti et al. [17] showed that addition of Ce^{3+} in the HFs confers an additional active corrosion protection by self-healing behavior which can be verified by the reduction of the corrosion rate compared to the HF without Ce^{3+} addition. Thus, considering the industrial potential which application of the coating, it is expected that the Ce^{3+} act to decreasing the corrosion process in the case of damage to the barrier layer.

The objective of this study is to evaluate the mechanical and electrochemical properties of galvanized steel coated with a HF obtained from an alkoxide precursor solution of 3-(trimethoxysilylpropyl) methacrylate (TMSPMA), cerium nitrate (0.01 M), and PEG plasticizer at a concentration of 60 g L^{-1} . The films were obtained by dip coating, with the application of either one (monolayer system) or two (bilayer system) layers. The films were cured at different temperatures (60 and 90°C) for 20 min.

2 Experimental procedures

2.1 Surface preparation

Galvanized steel substrates ($2 \text{ cm} \times 4 \text{ cm}$) were degreased by a 10 min immersion in neutral detergent at 70°C . The

Table 1 Description of the samples

Samples	Description
F3P60M	Galvanized steel coated with hybrid film cured at 60°C with application of monolayer
F3P60D	Galvanized steel coated with hybrid film cured at 60°C with application of bilayer
F3P90M	Galvanized steel coated with hybrid film cured at 90°C with application of monolayer
F3P90D	Galvanized steel coated with hybrid film cured at 90°C with application of bilayer
HDG	Galvanized steel without hybrid film

samples were rinsed with deionized water, dried, rinsed with ethanol and then dried once again. The galvanized layer composition used is 0.15C, 0.6Mn, 0.04S, 0.04P and the remainder is Zn (information was acquired from the supplier).

2.2 Elaboration of hybrid films

The hydrolysis reactions were conducted using the HF silane precursors TMSPMA ($\text{C}_{10}\text{H}_{20}\text{SiO}_5$) and tetraethoxysilane (TEOS; $\text{C}_8\text{H}_{20}\text{SiO}_4$) with the addition of 0.01 M cerium nitrate [17]. Ethanol and water were used as solvents. PEG 1500 was added to the sol formulation at a concentration of 60 g L^{-1} . In addition, a sample without plasticizer (PEG) was analyzed. The hydrolysis time was 24 h. Hydrolyzed hybrid solutions were applied by dip coating with an immersion time of 5 min and a removal rate of 10 cm min^{-1} . The films were obtained by dip coating. One or two layers were applied to the samples before they were dried and cured at different temperatures (60 and 90°C) for 20 min. Table 1 presents a description of the samples.

2.3 Experimental techniques

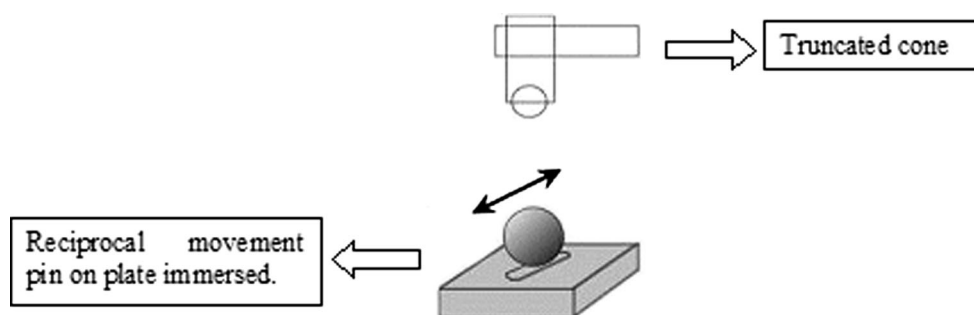
Morphological characterization was performed using a JEOL 6060 scanning electron microscopy (SEM) with an acceleration voltage of 20 kV. Top and cross-sectional views of the samples were used to determine layer thickness.

The surface micro-roughness was evaluated using a contact profilometer (PRO500 3D).

The wettability of the HFs was determined by contact angle measurements using the sessile drop method and equipment developed by the Laboratory of Corrosion Research (LAPEC) at UFRGS. The contact angle was determined using image analysis software.

The infrared (IR) spectroscopy measurements were performed on a Spectrum ASCII 100 spectrophotometer.

Fig. 1 Schematic representation of the tribologic test system



The measurements were performed with the mid-IR (4,000–500 cm^{-1}) beam. The spectra were obtained for the films without a substrate (free-standing films). For this characterization, two different curing temperatures (60 and 90 °C for 20 min) were analyzed.

The corrosion performance of the coatings was evaluated using open circuit potential (E_{OC}) monitoring, polarization curves, and electrochemical impedance spectroscopy (EIS) measurements in a 0.05 M of NaCl solution. This concentration is sufficiently high to activate corrosion in a relatively short period of time but low enough to determine the effects on the different samples. Kozhukharov et al. [18] also used 0.05 M of NaCl to ensure that the concentration was low enough to observe inhibitor effects. A three-electrode cell with a platinum wire counter electrode and SCE reference electrode was used to perform the analyses. The area of the working electrode was 0.626 cm^2 . The polarization curves were collected at a scan rate of 1 mV s^{-1} in a potential interval between 200 mV (below E_{OC}) and 400 mV (above E_{OC}). For the EIS measurements, the systems were monitored for 96 h. The amplitude of the EIS perturbation signal was 10 mV, and the frequency range studied was from 100 kHz to 10 mHz using a NOVA frequency response analyzer and an AUTOLAB PGSTAT 30 potentiostat.

The wear tests were performed with a computationally controlled tribometer using a ball-on-plate setting (Fig. 1). The wear test was conducted with reciprocal linear movement of an alumina sphere with a diameter 7.75 mm. A constant force of 1.5 N, frequency of 2 Hz and a track length of 2 mm were used.

3 Results and discussion

3.1 Morphological characterization

Figure 2 shows the SEM micrographs of the following HFIs prior to electrochemical testing: F3P60M, F3P60D, F3P90M, and F3P90D.

The SEM micrographs (Fig. 2) show the presence of cracks on the F3P90M and F3P90D HFIs, being more evident on the F3P90D bilayer systems. These results are consistent with several researchers [3, 19] who have reported that increased thickness, or additional layers, improves systems against corrosion. However, because of the fragile state of the thicker layers, microcracks in the morphological analysis and, consequently, a decrease in the corrosion resistance were observed. Moreover, as some authors have reported [16, 17], the formation of an irregular first layer impedes the formation of the second layer.

It was observed that the HFIs cured at 60 °C were not cracked. This may be attributed to the lower curing temperature, which did not cause cracking. However, dark spots were observed on the film, which was formed by residual solvent that did not evaporate during the curing process. This is related to the addition of PEG 1500 plasticizer. The molecular weight and increased viscosity of the PEG 1500 limited the evaporation of volatile organic compounds during curing after the application of the films [20].

The thickness of the film layers was determined by cross section SEM image analysis (Fig. 2), and the results are shown in Table 2.

The results (Fig. 2; Table 2) show that the F3P60D and F3P90D bilayer films had thicker layers compared to the F3P60M and F3P90M monolayer systems, as expected. The F3P60D bilayer system, which was cured at a temperature of 60 °C, had the thickest layers. This result indicates that a temperature of 60 °C enabled the formation of thick films, however, the presence of residual solvent inside these films can compromise the effectiveness of the barrier against corrosion.

The introduction of PEG in the sol formulation increases the coating thickness and limits solvent evaporation during the curing process. Therefore, the barrier effect is obtained predominately because of the hydration and/or saturation of solvents in the applied layers. Thus, for each layer, time and temperature must be adapted and optimized to form denser films that perform well and enhance the effectiveness of the barrier against corrosion [21].

Fig. 2 Layer thickness obtained for the hybrid films: **a** F3P60M, **b** F3P60D, **c** F3P90M, and **d** F3P90D

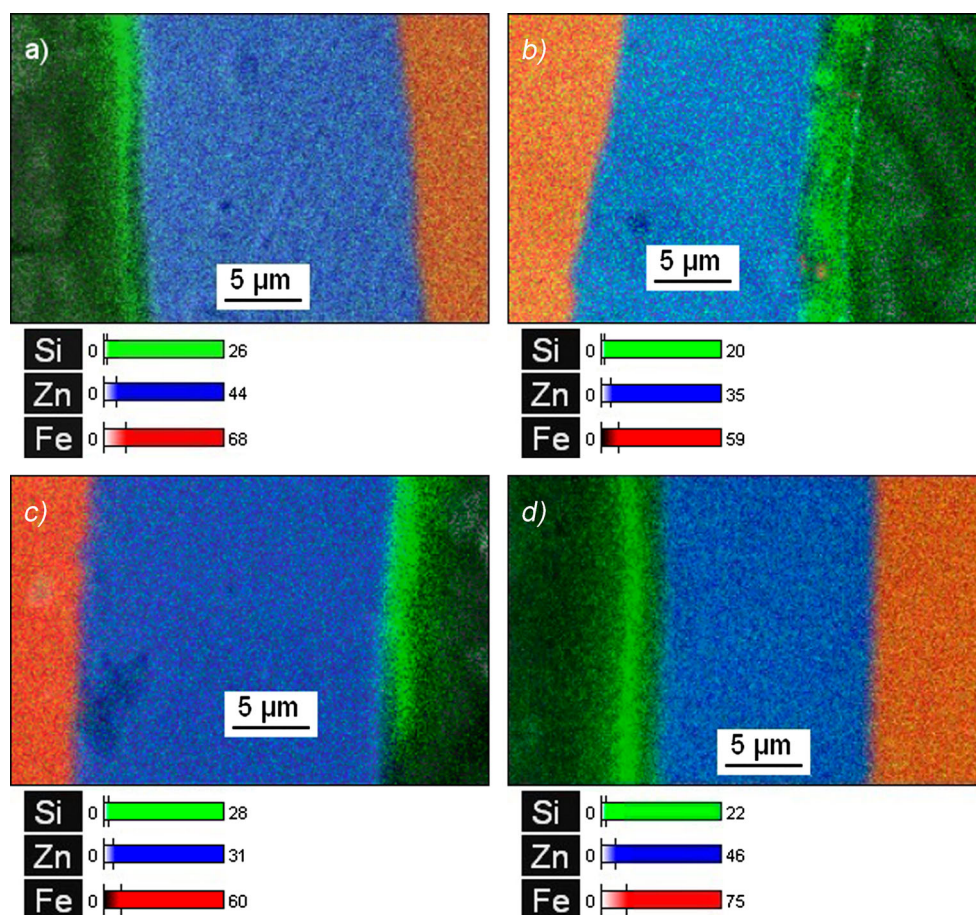


Table 2 Results of the layer thickness, contact angle, and roughness for the hybrid films studied

Samples	Thickness (μm)	Contact angle	Surface roughness		
			R_a (μm)	R_{ms} (μm)	R_z (μm)
F3P60M	1.87 ± 0.34	$73^\circ \pm 2.19$	1.20 ± 0.15	1.53 ± 0.16	8.94 ± 0.18
F3P60D	4.16 ± 0.42	$80^\circ \pm 1.37$	1.16 ± 0.12	1.45 ± 0.12	8.86 ± 0.24
F3P90M	2.45 ± 0.38	$72^\circ \pm 1.58$	1.32 ± 0.13	1.59 ± 0.19	8.61 ± 0.16
F3P90D	3.33 ± 0.56	$76^\circ \pm 0.86$	1.08 ± 0.11	1.36 ± 0.18	8.08 ± 0.28
HDG	–	$66^\circ \pm 5.33$	1.35 ± 0.12	1.60 ± 0.15	9.27 ± 0.26

Thicker monolayer systems were cured at 90 °C. This is because excess heat in the curing process increases the number of cross-linking silane reactions, which reduces reactivity. This loss of reactivity is caused by the conversion of the silanol groups to siloxanes. As a result, the film becomes dense and reactions with subsequent layers become more difficult [22].

Figure 3 shows three-dimensional (3D) images that were obtained by profilometry for all of the studied systems, including images of uncoated galvanized steel. The obtained roughness values are shown in Table 2.

According to the data, all of the HFs studied had smaller roughness [23] values than uncoated galvanized steel.

Therefore, these results confirm the development of a new formulation. By introducing a plasticizer, the thickness of the layers increased to form an even and homogeneous coating on galvanized steel, which has an extremely heterogeneous roughness.

The contact angle measurements obtained for the studied systems and HDG are listed in Table 2. The totality of HFs had a higher contact angle and lower wettability compared to the uncoated galvanized steel.

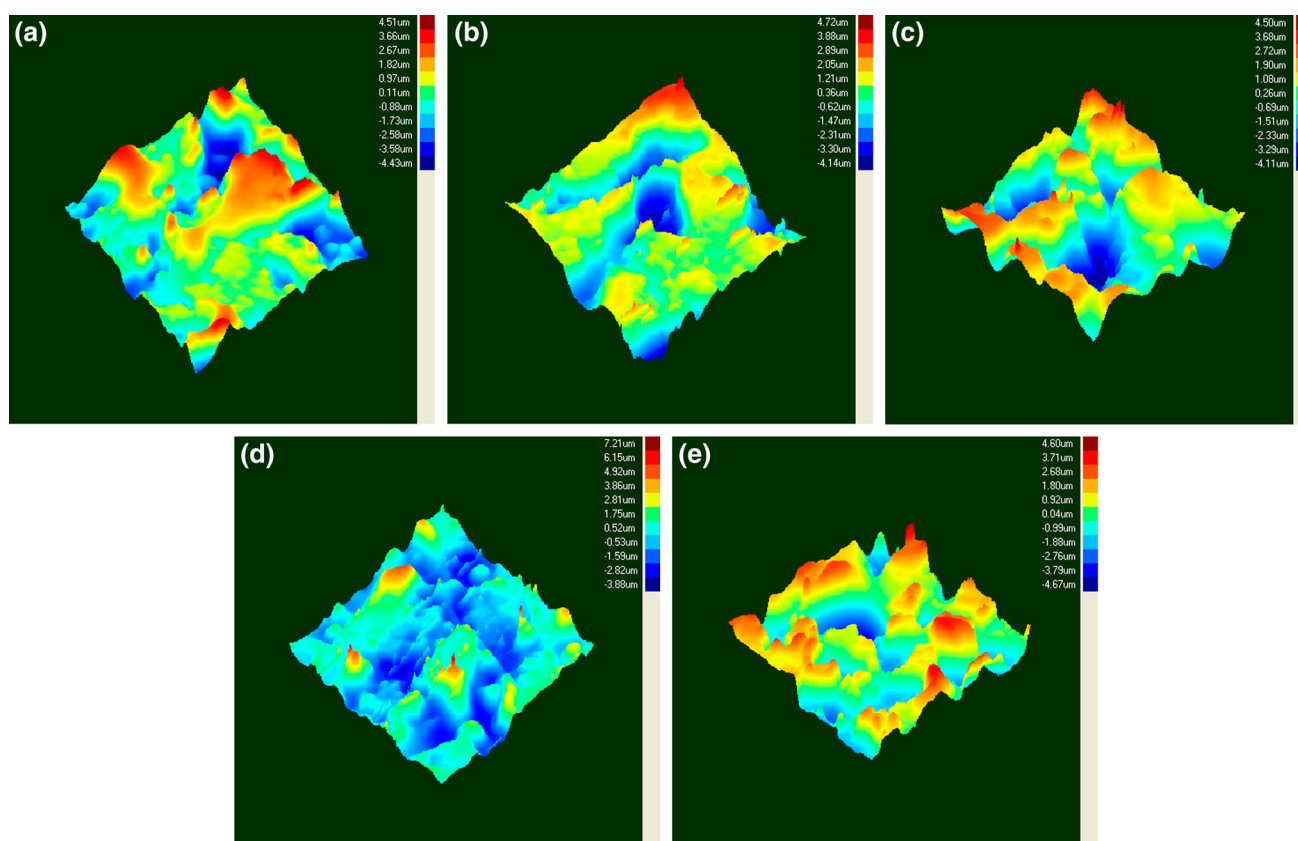


Fig. 3 3D images profilometry obtained by: **a** F3P60M, **b** F3P60D, **c** F3P90M, **d** F3P90D, and **e** HDG uncoated

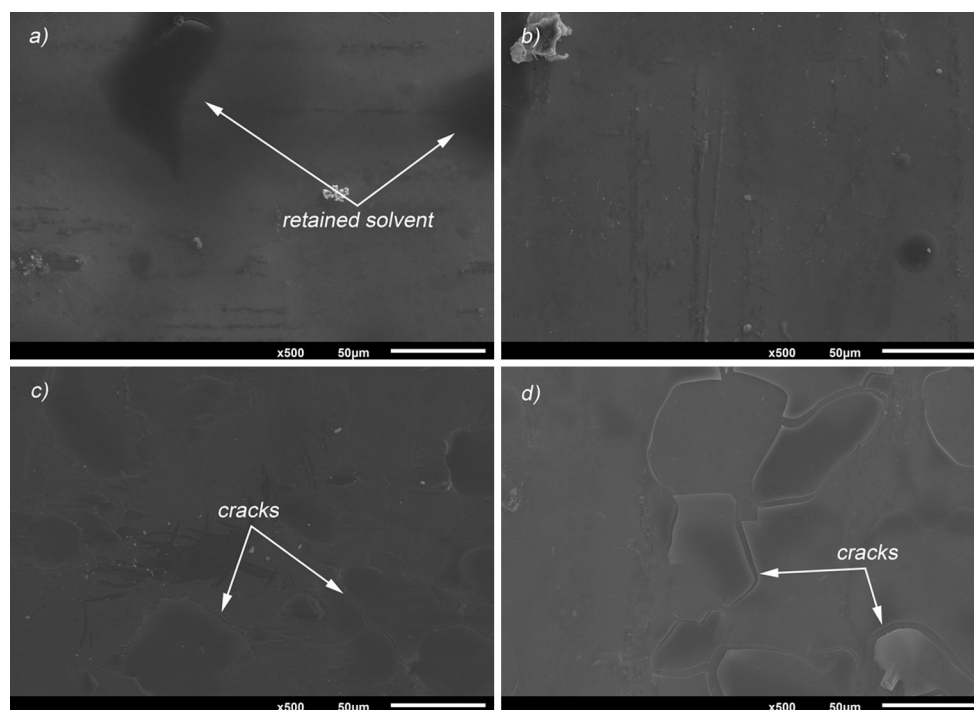


Fig. 4 SEM micrographs for the systems: **a** F3P60M, **b** F3P60D, **c** F3P90M, and **d** F3P90D

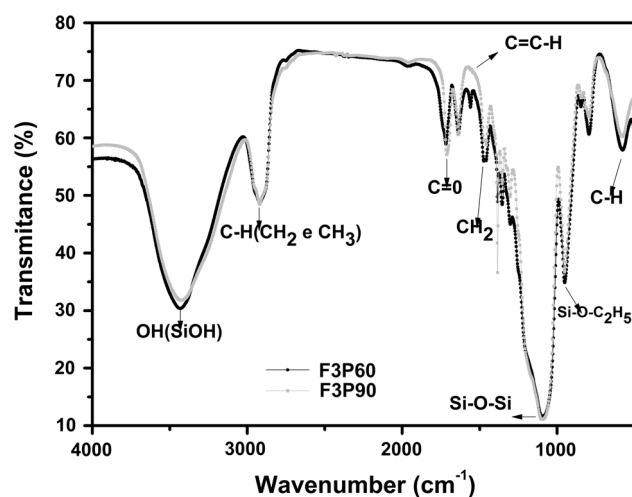


Fig. 5 FT-IR spectra of the hybrid films formulated with the different temperatures (F3P60 and F3P90)

In analyzing the HFs, the bilayer films displayed higher contact angles than the monolayer films. This is explained because the thicker the layer, the more difficult it is for water infiltration to occur. This suggests that layers that are completely polymerized are denser. Thus, the pore volume is lower and water cannot easily penetrate the structure, i.e., the films are less hydrophilic. Moreover, a larger contact angle was obtained for the F3P60D system, which showed no cracks from film formation, as shown in SEM micrographs (Fig. 4).

Figure 5 and Table 3 present the FT-IR spectrum of the HFs prepared with different temperatures (60 and 90 °C). In Fig. 7, strong bands between 1,000 and 1,200 cm^{-1} are attributed to Si–O–Si, the structural backbone of the hybrid material. The formation of the Si–O–Si layer protects the tin plate substrate. The bands at intermediate frequencies, between 900 and 960 cm^{-1} , are attributed to the Si–OCH₂CH₃ group from the incomplete hydrolysis of TEOS. Peaks at approximately 2,900 cm^{-1} were identified and are associated with symmetrical and asymmetrical –CH stretching (CH₂ and CH₃) in the aliphatic chain of the organosilane (TMSPMA). All of these peaks are present in the spectra of the prepared HFs, which suggests that different temperatures do not affect HF formation and that complete hydrolysis and the subsequent crosslinking of these samples occurred. The broad absorption between 3,200 and 3,700 cm^{-1} is characteristic of the axial deformation of –OH, which could arise from silanol groups (Si–OH) that were not condensed during synthesis. In this case, the peak intensities of the two samples were similar, indicating that a temperature of 60 °C was enough to initiate cross-linking reactions. The bands at approximately 1,728 and 1,622 cm^{-1} are attributed to the stretching vibrations of C=O and C=C groups, respectively.

Table 3 FT-IR, peaks assignment as function of peak position [22]

Peak positions (cm^{-1})	Peak assignment
600–700	C–H (Si–CH ₂ –CH ₂ –Si) stretching
900–960	Unhydrolyzed Si–O–C ₂ H ₅ asymmetrical stretching
1,000–1,200	Si–O–Si crosslinked Si–O stretching
1,300–1,400	CH ₂ and CH ₃ scissoring
1,600–1,670	C=C–H axial deformation
1,700–1,750	C=O axial deformation
2,900–3,000	C–H (CH ₂ –CH ₃) symmetric and asymmetric stretchings
3,200–3,700	Si–OH axial deformation

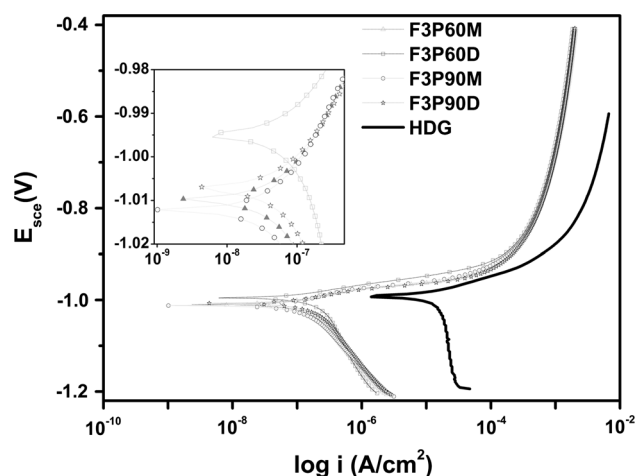


Fig. 6 Polarization curves for the films F3P60M, F3P60D, F3P90M, and F3P90D and for uncoated galvanized steel

Table 4 Obtained data from Tafel extrapolation

Samples	i_{corr} (A cm^{-2})	E_{corr} (mV)	R_p ($\Omega \text{ cm}^2$)
F3P60M	2.03×10^{-7}	–1,003	6.75×10^4
F3P60D	1.99×10^{-7}	–988	5.16×10^4
F3P90M	5.48×10^{-7}	–1,000	2.02×10^4
F3P90D	1.91×10^{-7}	–1,009	7.92×10^4
HDG	4.07×10^{-5}	–992	6.41×10^3

3.2 Electrochemical characterization

In Fig. 6, potentiodynamic polarization curves are shown for the studied samples. The corrosion current density (i_{corr}), corrosion potential (E_{corr}), and polarization resistance (R_p) were determined from Tafel slope extrapolation. The results are shown in Table 4.

The results show that all of the HFs studied promoted an increase (two orders of magnitude higher) in R_p and a decrease (two orders of magnitude lower) in corrosion

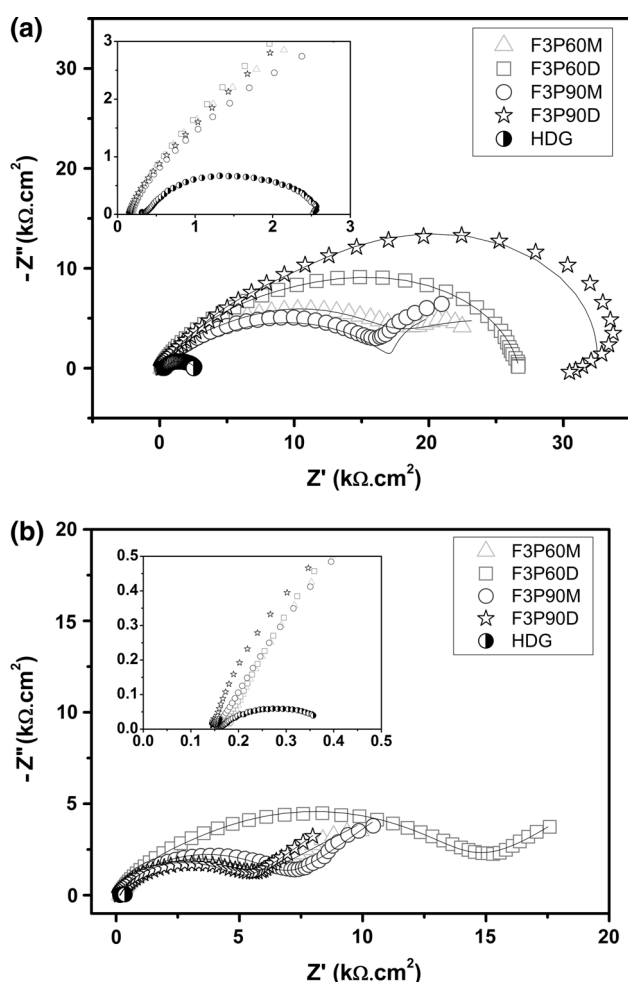


Fig. 7 Nyquist diagrams obtained for uncoated galvanized steel and post-treated with the hybrid films in 0.05 M of NaCl for **a** 24 h and **b** 96 h of immersion. The quality of these fits can be verified by the continuous lines

current density (i_{corr}) compared to the galvanized steel, indicating the protective performance of these films. As reported by Bastos et al. [24], the condensation of tetrafunctional alkoxides was retarded due to the presence of PEG. The increased steric hindrance in the transition state promoted a more flexible film with increased adhesion to the substrate and improved anticorrosive properties of the coating.

Nevertheless, a significant difference between the HFs was not observed. By zooming the graph in, it is observed that the monolayer HFs (F3P90M and F3P60M) have more active corrosion potentials than the F3P60D sample, which was the thickest film without crack formation.

The Nyquist diagrams for the F3P60M, F3P60D, F3P90M, and F3P90D films and the uncoated galvanized steel were obtained from electrochemical impedance assays performed at 24 and 96 h in a solution of 0.05 M of NaCl and are shown in Fig. 7.

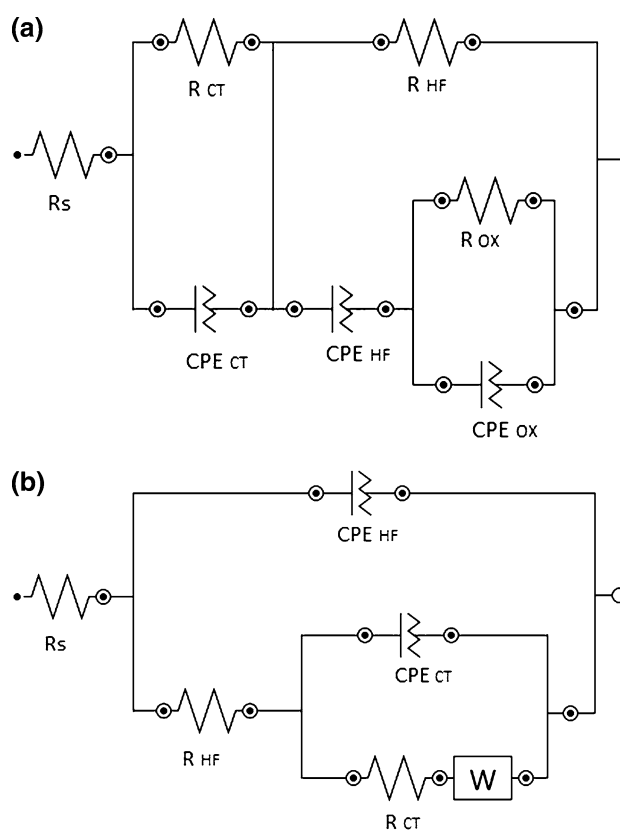


Fig. 8 Equivalent circuit **a** samples F3P60M and F3P60D (at all times studied) F3P90M and F3P90D (up to 72 h) and **b** samples F3P90M and F3P90D (at 96 h of immersion)

Although the Nyquist plots (Fig. 7) appear to be similar in shape for 96 h (Fig. 7b) they differ in size. This suggests that the same fundamental phenomenon could have occurred in all these coatings but over a different effective areas [25].

The diameter of the arch can be regarded as the coating R_p [26]. Moreover, the bilayer coatings that were immersed in the solution for 24 h showed the largest semicircle (Fig. 7a). At the end of the test, the F3P60D sample retained the highest resistance values, whereas the F3P90D system showed similar resistance values to the monolayer systems. This is due to the F3P90D sample having developed cracks on the film, as observed in the SEM images (Fig. 4d).

Therefore, the number of layers must be adjusted to the film curing temperature. Simply increasing the thickness of the film (Fig. 2; Table 2) does not guarantee improved corrosion resistance. Besides, the embrittlement of thick layers causes the formation of cracks, which reduces corrosion resistance [24].

However, all of the HFs that were studied presented much higher resistance values at 24 and 96 h of immersion than the uncoated galvanized steel. Furthermore, the

Table 5 Electrical elements fitted values for F3P60M film up to 96 h of immersion in 0.05 M of NaCl solution

Time (h)	R_S ($\Omega \text{ cm}^2$)	R_{HF} ($k\Omega \text{ cm}^2$)	CPE_{HF} ($\mu F \text{ cm}^2$)	n_{HF}	R_{OX} ($k\Omega \text{ cm}^2$)	CPE_{OX} ($\mu F \text{ cm}^2$)	n_{OX}	R_{CT} ($k\Omega \text{ cm}^2$)	CPE_{CT} ($\mu F \text{ cm}^2$)	n_{CT}
24	281 (0.9)	5.55 (8.4)	7.24 (2.2)	0.84 (8.8)	26.95 (4.5)	13.2 (8.9)	0.80 (6.7)	51.15 (7.3)	352 (6.7)	0.67 (4.6)
48	285 (1.3)	2.28 (2.1)	8.25 (3.3)	0.85 (9.4)	10.23 (4.2)	12.5 (4.0)	0.84 (3.1)	40.93 (2.0)	290 (6.5)	0.52 (6.8)
72	274 (1.4)	2.13 (9.3)	8.24 (3.0)	0.85 (9.7)	8.61 (4.3)	14.2 (5.4)	0.85 (3.0)	53.91 (5.8)	333 (3.0)	0.49 (5.6)
96	271 (1.5)	1.77 (9.4)	8.72 (5.6)	0.90 (9.5)	7.76 (3.6)	14.6 (4.9)	0.85 (9.5)	109.76 (8.2)	349 (9.2)	0.46 (4.6)

The error % associated to each parameter value is given in parenthesis

Table 6 Electrical elements fitted values for F3P60D film up to 96 h of immersion in 0.05 M of NaCl solution

Time (h)	R_S ($\Omega \text{ cm}^2$)	R_{HF} ($k\Omega \text{ cm}^2$)	CPE_{HF} ($\mu F \text{ cm}^2$)	n_{HF}	R_{OX} ($k\Omega \text{ cm}^2$)	CPE_{OX} ($\mu F \text{ cm}^2$)	n_{OX}	R_{CT} ($k\Omega \text{ cm}^2$)	CPE_{CT} ($\mu F \text{ cm}^2$)	n_{CT}
24	274 (0.7)	4.02 (8.9)	7.83 (6.3)	0.76 (1.5)	14.42 (9.5)	6.89 (4.8)	0.90 (5.5)	42.32 (5.5)	11.40 (5.2)	0.89 (5.8)
48	270 (1.2)	3.38 (3.9)	5.55 (6.5)	0.87 (9.7)	22.48 (9.1)	217 (5.1)	0.53 (5.9)	42.28 (9.3)	7.00 (9.0)	0.81 (9.4)
72	257 (1.6)	2.91 (6.5)	4.56 (9.8)	0.90 (7.9)	8.68 (8.4)	343 (9.8)	0.40 (6.6)	24.78 (9.4)	7.48 (7.6)	0.81 (3.6)
96	239 (1.6)	2.79 (5.7)	5.39 (9.5)	0.87 (7.6)	9.90 (9.7)	362 (8.3)	0.39 (5.9)	27.90 (4.8)	8.56 (7.3)	0.78 (3.4)

The error % associated to each parameter value is given in parenthesis

F3P60D sample (Table 6) exhibited a resistance value that was 17 times higher than the uncoated substrate and more than 40 times higher than the uncoated substrate after 24 and 96 h of immersion in 0.05 M of NaCl solution, respectively, which demonstrates the protective action of this HF against the corrosion of galvanized steel (Table 9).

EIS was used in order to characterize the corrosion behavior of the developed coatings in the present work. A detailed interpretation of the EIS measurements was performed by fitting the experimental plots with equivalent electrical circuit models, which simulated the electrochemical behavior of the studied coatings (Fig. 8). These models were based on the combination of resistances, capacitances, and other elements with a physical significance related to the electrochemical response of the system.

Tables 5, 6, 7, 8 and 9 present the electrical parameters that were obtained by fitting the equivalent electrical circuits from the experimental EIS data of the F3P60M, F3P90M, F3P60D, and F3P90D HFs after 96 h of immersion in a 0.05 M of NaCl solution. It was not possible to fit impedance curves to the HFs during the first hour of immersion because they were unstable in the solution. These instabilities in the first few hours of the EIS experiments may be correlated with the modification of the E_{OC} that was observed during the initial immersion period [27]. These results are related to the interaction of the electrolyte with the film, such as the permeation of the electrolyte through the film, which is not an instant process. Other authors [18, 28] have found similar results and only present EIS data after several hours of immersion.

In several circuits, the capacitance was substituted by a constant phase element (CPE) to consider the non-ideality of the systems. In these circuits (Fig. 8), R_S represents the electrolyte resistance, R_{HF} is the resistance, and CPE_{HF} is a constant phase element associated with the effectiveness of the HF as a resistant barrier. In the same circuit, R_{OX} and CPE_{OX} represent, respectively, the resistance and the constant phase element that indicate the acceleration of interfacial processes associated with the presence of zinc oxide on the substrate surface. R_{CT} and CPE_{CT} were added and represent the charge transfer resistance of the metal.

The same equivalent circuit model (Fig. 8) was proposed to simulate the electrochemical behavior of the F3P60M, F3P60D, F3P90M, and F3P90D samples at all immersion times (24, 48, 72, and 96 h). Three time constants (Fig. 8a) were revealed for the F3P60M and F3P60D samples (in all of the times studied) and for the F3P90M and F3P90D samples (for up to 72 h). The first time constant was observed at a high frequency, and it is associated with the barrier resistance of the HF. The second time constant was detected at a medium frequency range of elements, and it is attributed to the presence of an OX on the metal/coating interface. Finally, the third time constant was located in a low frequency range, and it is associated with the CT of the metal [29, 30]. This behavior was also observed by other authors [31, 32].

However, at 96 h of immersion, the barrier properties of the F3P90M and F3P90D coating deteriorated, and corrosion activities were observed on the substrate. Therefore, an equivalent scheme was substituted for the circuit, as shown in Fig. 8b.

Table 7 Electrical elements fitted values for F3P90M film up to 96 h of immersion in 0.05 M of NaCl solution

Time (h)	R_S ($\Omega \text{ cm}^2$)	R_{HF} ($k\Omega \text{ cm}^2$)	CPE_{HF} ($\mu\text{F cm}^2$)	n_{HF}	R_{OX} ($k\Omega \text{ cm}^2$)	CPE_{OX} ($\mu\text{F cm}^2$)	n_{OX}	R_{CT} ($k\Omega \text{ cm}^2$)	CPE_{CT} ($\mu\text{F cm}^2$)	n_{CT}
24	281 (1.5)	3.48 (7.1)	6.00 (8.0)	0.87 (8.4)	8.60 (3.9)	13.2 (4.5)	0.63 (2.8)	13.13 (3.5)	760 (3.1)	0.90 (9.9)
48	236 (1.8)	3.39 (7.9)	5.54 (9.1)	0.83 (8.2)	14.36 (3.4)	12.1 (3.4)	0.74 (2.5)	27.10 (8.3)	280 (3.4)	0.46 (5.5)
72	232 (2.0)	2.33 (6.6)	5.69 (8.8)	0.86 (6.5)	10.63 (2.1)	8.54 (7.9)	0.85 (8.3)	24.30 (9.7)	285 (8.9)	0.42 (3.9)
W ($\mu\text{F cm}^2$)										
96	236 (1.5)	2.49 (4.4)	7.67 (1.8)	0.73 (5.6)	10.11 (2.9)	9.00 (9.6)	0.90 (3.9)		448 (3.9)	

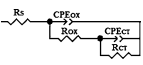
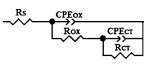
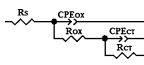
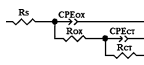
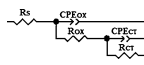
The error % associated to each parameter value is given in parenthesis

Table 8 Electrical elements fitted values for F3P90D film up to 96 h of immersion in 0.05 M of NaCl solution

Time (h)	R_S ($\Omega \text{ cm}^2$)	R_{HF} ($k\Omega \text{ cm}^2$)	CPE_{HF} ($\mu\text{F cm}^2$)	n_{HF}	R_{OX} ($k\Omega \text{ cm}^2$)	CPE_{OX} ($\mu\text{F cm}^2$)	n_{OX}	R_{CT} ($k\Omega \text{ cm}^2$)	CPE_{CT} ($\mu\text{F cm}^2$)	n_{CT}
24	240 (0.9)	2.34 (4.6)	8.66 (5.6)	0.84 (9.3)	22.44 (8.2)	9.85 (3.2)	0.85 (3.1)	51.64 (8.1)	25.2 (2.9)	0.90 (3.7)
48	242 (1.0)	2.25 (9.7)	8.63 (5.9)	0.89 (5.5)	16.25 (6.6)	13.6 (4.2)	0.84 (7.2)	42.9 (7.9)	79.1 (3.8)	0.76 (9.9)
72	240 (1.4)	1.44 (4.1)	8.25 (3.2)	0.90 (6.5)	9.48 (8.0)	59.0 (3.0)	0.55 (2.9)	14.67 (9.3)	17.8 (4.8)	0.82 (3.4)
W ($\mu\text{F cm}^2$)										
96	218 (2.3)	1.39 (8.3)	11.0 (3.9)	0.77 (5.6)	7.40 (7.8)	24.0 (8.5)	0.90 (5.2)		547 (6.2)	

The error % associated to each parameter value is given in parenthesis

Table 9 Electrical elements fitted values for HDG up to 96 h of immersion in a 0.05 M of NaCl solution

HDG	1 h	24 h	48 h	72 h	96 h
Fitted circuit					
R_S ($\Omega \text{ cm}^2$)	151.0 (0.9)	150.8 (1.4)	148.5 (1.1)	151.3 (1.3)	146.9 (1.2)
CPE_{OX} (F cm^{-2})	1.0×10^{-6} (10.8)	1.08×10^{-4} (3.2)	2.80×10^{-4} (9.8)	2.41×10^{-4} (2.0)	2.29×10^{-4} (8.9)
n_{OX}	0.75 (2.6)	0.74 (8.1)	0.66 (8.1)	0.90 (9.5)	0.80 (9.1)
R_{OX} ($\Omega \text{ cm}^2$)	466 (3.2)	468 (3.1)	252 (7.3)	192 (8.7)	178 (9.9)
CPE_{CT} (F cm^{-2})	6.53×10^{-3} (2.2)	6.5×10^{-3} (2.7)	14.6×10^{-3} (6.8)	1.6×10^{-3} (6.1)	3.67×10^{-3} (3.1)
n_{CT}	0.82 (5.1)	0.81 (6.3)	0.90 (7.6)	0.30 (9.3)	0.55 (3.6)
R_{CT} ($\Omega \text{ cm}^2$)	1,085 (7.2)	1,155 (0.9)	956 (5.6)	1,231 (2.1)	867 (2.8)

The proposed equivalent circuit displays a section in the high frequency range that is associated with the HF, and another section in the low frequency range that is associated with the CT of the metal and the Warburg finite impedance, W . The Warburg impedance and the CPE are used to model the increasing ionic conductivity due to corrosion inside the cracks [33, 34].

The resistance (R_{HF}) of the HF can be estimated from Nyquist diagrams using the semicircle diameter at high frequencies. Moreover, values of approximately 4–5.55 $k\Omega \text{ cm}^2$ were obtained for the F3P60M and F3P90D samples at 24 h of immersion (Tables 5, 6, 7, 8). After that, a decrease in

impedance was observed, being more significant for the F3P60D system.

Figures 9 and 10 show the evolution of the coating properties (i.e. the resistance and capacitance, respectively) as a function of immersion time. Generally, the high-frequency resistance values (Fig. 9) decreased during the first hours of immersion; this occurred more significantly for the F3P60M HF. According to previous analysis by several authors, this may be attributed to the development of conductive pathways inside thin-layered HFs [35]. The F3P60D sample exhibited the highest resistance after 48 h of immersion (Fig. 9) compared to the other samples

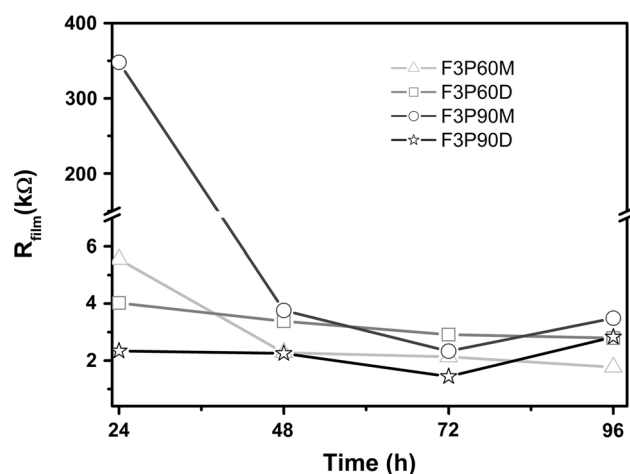


Fig. 9 Evolution of the hybrid films resistance for F3P60M, F3P60D, F3P90M, and F3P90D in a 0.05 M of NaCl solution with the immersion time

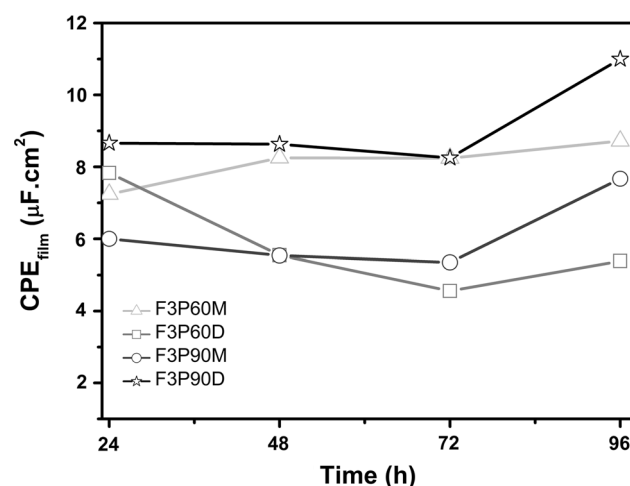


Fig. 10 Evolution of the hybrid films constant phase element capacitance for F3P60M, F3P60D, F3P90M, and F3P90D in a 0.05 M of NaCl solution with the immersion time

(F3P60M, F3P90M, and F3P90D). This is associated with the formation of a thicker film layer (Fig. 2; Table 2) and, consequently, good crosslinking. Therefore, the curing temperature (60 °C) enabled the formation of a dense, hydrophobic film (as shown by the contact angle results in Table 2, and the FT-IR results in Fig. 5; Table 3).

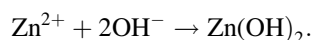
The evolution of coating resistance is a major characteristic of the barrier properties of a protective layer [36]. The F3P90M and F3P90D samples showed a sharp reduction in resistance from 48 to 72 h of immersion; this may be attributed to the presence of cracks and irregularities from the formation of these HFs, as shown by SEM micrographs (Fig. 4). Subsequently, the resistance of the F3P60D coating decreased slowly over an immersion time of 96 h, which reflects the stability and good barrier

properties of the coating [30]. In contrast, the barrier properties of the F3P60M coating rapidly declined after 48 h of immersion. This rapid decrease is related to the formation of new defects and pores in the coatings [30].

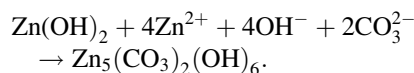
In Fig. 10, it is observed that the F3P60D sample had a smaller capacitance than the other samples until the end of the test, which indicates the performance barrier properties of the HF. Furthermore, there was an increase in the capacitance of the F3P90M and F3P90D coatings after 72 h of immersion, which can be explained by a reduction in the coating thickness and/or conductivity and, hence, an increase in the porosity [29].

For the F3P90M sample, a slight increase in capacitance (Fig. 10) was observed at 48 h of immersion, which is associated with the electrolyte absorption. After 96 h of immersion, another small, yet significant, increase in the capacitance of the film was observed as a result of water absorption, which reduced the barrier properties of the film [33].

For the uncoated galvanized steel (Table 9), two time constants were observed over the entire immersion time (1, 24, 48, 72, and 96 h). This phenomenon at low frequency may be related to the R_{CT} of the metal. The response of the CT shifted to lower frequencies as the active area expanded, which increased the capacitance. Another process with very low resistance was observed at medium frequency, which is associated with zinc oxide on the substrate surface and may result from cathodic reactions or the precipitation of zinc hydroxide, as shown below [37].



According to the Pourbaix diagram for zinc, at pH values above 8, zinc hydroxide is stable—a value that is easily attainable for steel. Additionally, carbonate can also be formed, which generates hydrozincite, as shown below [38]:



The majority of publications that apply impedance to corrode systems use continuous metals and not galvanic couples. In such systems, the interpretation of the impedance spectrum may be facilitated by the results of the separate metals. It is interesting to note that at 96 h of immersion, the HDG showed a lower resistance and a higher capacitance (Table 9) in comparison to the HFs (Tables 5, 6, 7, 8).

Figure 11 shows the SEM micrographs of films after 96 h of electrochemical impedance testing submerged in a 0.05 M of NaCl solution. As expected, the F3P60D sample (Fig. 11b) produced less corrosion products compared to the other films because of its good performance in the electrochemical impedance test. Regardless, all HFs

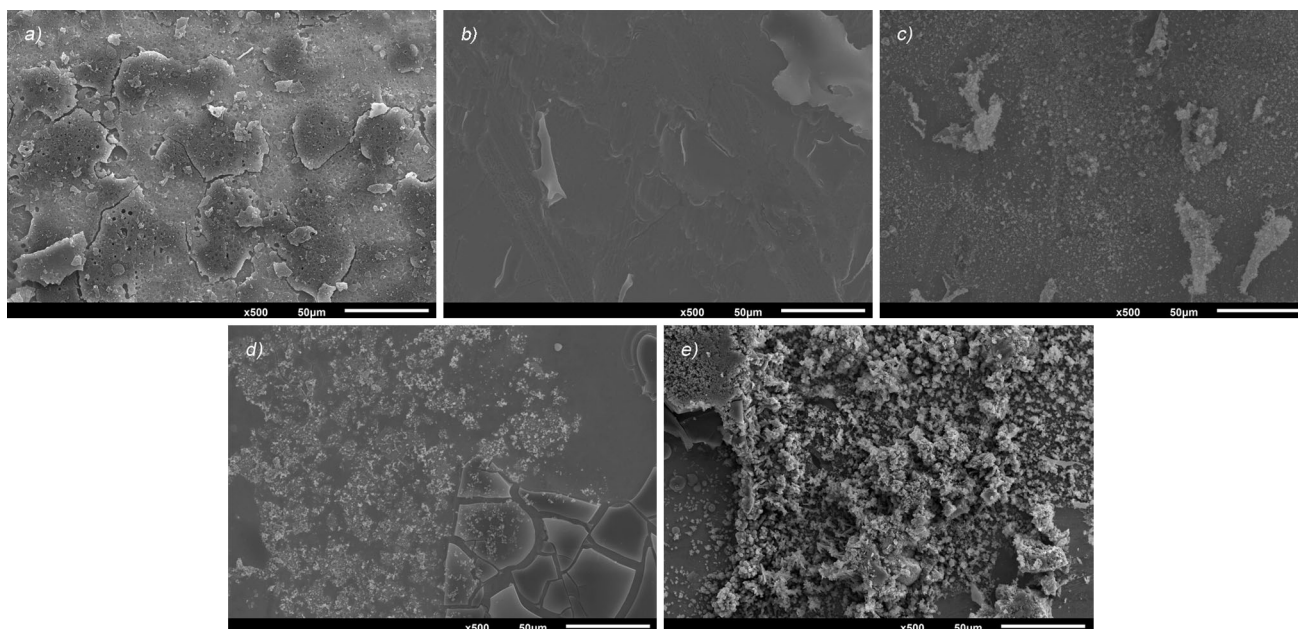


Fig. 11 Images obtained after 96 h of electrochemical impedance for the samples **a** F3P60M, **b** F3P60D, **c** F3P90M, **d** F3P90D, and **e** HDG

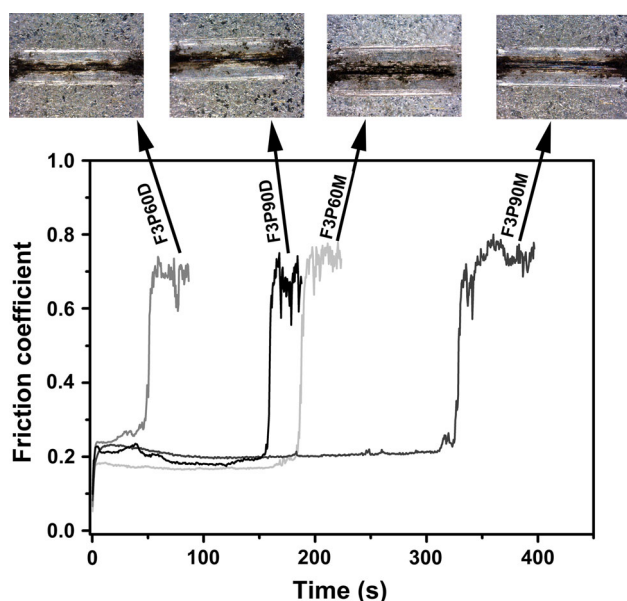


Fig. 12 Coefficient of friction of the hybrid films F3P60M, F3P60D, F3P90M, and F3P90D

produced less corrosion products than the uncoated galvanized steel.

3.3 Mechanical characterization

Figure 12 shows the coefficient of friction (COF) with time for the samples. As observed, the bilayer systems performed worse than the monolayer systems in the wear test. This is attributed to the film adhesion. For monolayer

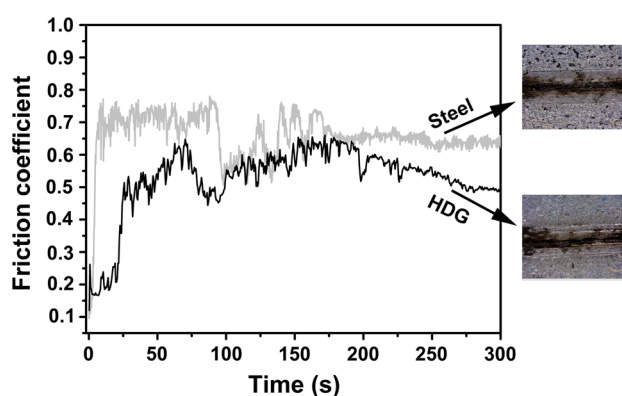


Fig. 13 Coefficient of friction of the galvanized steel without coating and steel

systems, the film tends to adhere firmly to the substrate; however, when a second layer is added, there is a loss in reactivity of the first layer due to condensation reactions that occur during the gel formation stage, which weakens the interactions between the layers and reduces the adhesion of the second layer.

After comparing the effect of curing temperature, the systems cured at 90 °C were found to have a higher wear resistance than samples cured at 60 °C. This may be because the excess of heat during the curing process causes an increase in “cross-linking” silane reactions and the formation of siloxane groups, which are responsible for forming protective, hydrophobic layers with reduced reactivity and increased mechanical strength. The loss in reactivity is caused by the conversion of the silanol groups to siloxanes [22].

The change in the COF in Fig. 13 determines the exchange of the tribological pair, i.e., the ruptured film and the iron (Fe) and the galvanized steel (HDG) substrates. As observed in Figs. 12 and 13, the COF for the samples with HF's stabilized close to the COF of Fe ($\mu = 0.7$) after film fragmentation. This indicates that the films strongly adhered to Zn; upon breakage of the HF, the Zn film also breaks. The similarities between the HDG and F3P60D samples can be observed in Figs. 12 and 13.

4 Conclusions

The study realized showed that the HF's cured at 60 °C presented homogeneous surface, whereas the HF's cured at 90 °C presented surface with cracks. The bilayer films presented thicker layers compared to the monolayer systems. All the HF's studied had roughness values smaller, contact angle higher and wettability lower when compared to the uncoated galvanized steel.

EIS showed that F3P60D sample presented highest resistance values when compared to the other samples. However, all of the HF's that were studied presented much higher resistance values than the uncoated galvanized steel.

In the wear test, the bilayer systems performed worse than the monolayer systems in the wear test. This is due the film adhesion, because, in the monolayer systems, the film tends to adhere firmly to the substrate; when comparing the effect of curing temperature, the systems cured at 90 °C presented higher wear resistance than samples cured at 60 °C.

Based on the results presented, it is concluded that sample cured at 60 °C with a bilayer exhibited the best electrochemical tests performance; whereas, the sample cured at 90 °C with monolayer showed better mechanical performance compared to other samples.

Acknowledgments The authors would like to thank CAPES (the Brazilian Government Agency for the Development of Human Resources) and CNPq (the Brazilian National Council for Scientific and Technological Development) for the financial support.

References

- Zhu D, van Ooij WJ (2003) Corrosion protection of AA 2024-T3 by bis-[3-(triethoxysilyl)propyl]tetrasulfide in sodium chloride solution: Part 2: mechanism for corrosion protection. *Corros Sci* 45:2177–2197. doi:10.1016/S0010-938X(03)00061-1
- Seth A, van Ooij WJ, Puomi P et al (2007) Novel, one-step, chromate-free coatings containing anticorrosion pigments for metals—an overview and mechanistic study. *Prog Org Coat* 58:136–145. doi:10.1016/j.porgcoat.2006.08.030
- Vanin FM, Sobral PJA, Menegalli FC et al (2005) Effects of plasticizers and their concentrations on thermal and functional properties of gelatin-based films. *Food Hydrocoll* 19:899–907. doi:10.1016/j.foodhyd.2004.12.003
- Liu J, Zhan Z, Yu M, Li S (2013) Adsorption behavior of glycidoxypentyl-trimethoxy-silane on titanium alloy Ti-6.5Al-1Mo-1V-2Zr. *Appl Surf Sci* 264:507–515. doi:10.1016/j.apsusc.2012.10.054
- Rahimi H, Mozaffarinia R, Hojjati Najafabadi A (2013) Corrosion and wear resistance characterization of environmentally friendly sol-gel hybrid nanocomposite coating on AA5083. *J Mater Sci Technol* 29:603–608. doi:10.1016/j.jmst.2013.03.013
- Zheludkevich ML, Serra R, Montemor MF et al (2006) Corrosion protective properties of nanostructured sol-gel hybrid coatings to AA2024-T3. *Surf Coat Technol* 200:3084–3094. doi:10.1016/j.surfcoat.2004.09.007
- Metrok TL, Parkhill RL, Knobbe ET (2001) Passivation of metal alloys using sol-gel-derived materials—a review. *Prog Org Coat* 41:233–238. doi:10.1016/S0300-9440(01)00134-5
- Meth S, Savchenko N, Viva FA et al (2011) Siloxane-based thin films for corrosion protection of stainless steel in chloride media. *J Appl Electrochem* 41:885–890. doi:10.1007/s10800-011-0291-2
- Pantoja M, Díaz-Benito B, Velasco F et al (2009) Analysis of hydrolysis process of γ -methacryloxypropyltrimethoxysilane and its influence on the formation of silane coatings on 6063 aluminum alloy. *Appl Surf Sci* 255:6386–6390. doi:10.1016/j.apsusc.2009.02.022
- Wang D, Bierwagen GP (2009) Sol-gel coatings on metals for corrosion protection. *Prog Org Coat* 64:327–338. doi:10.1016/j.porgcoat.2008.08.010
- Costa E (1998) Preparação e caracterização de filmes finos sol-gel de Nb₂O₅-TiO₂. Universidade de São Paulo, São Paulo
- Yang L, Feng J, Zhang W, Qu J (2010) Film forming kinetics and reaction mechanism of γ -glycidoxypentyltrimethoxysilane on low carbon steel surfaces. *Appl Surf Sci* 256:6787–6794. doi:10.1016/j.apsusc.2010.04.090
- Certhoux E, Ansart F, Turq V et al (2013) New sol-gel formulations to increase the barrier effect of a protective coating against the corrosion of steels. *Prog Org Coat* 76:165–172. doi:10.1016/j.porgcoat.2012.09.002
- Li G, Wang X, Li A et al (2007) Fabrication and adhesive properties of thin organosilane films coated on low carbon steel substrates. *Surf Coat Technol* 201:9571–9578. doi:10.1016/j.surfcoat.2007.04.032
- Honkanen M, Hoikkanen M, Vippola M et al (2011) Characterization of silane layers on modified stainless steel surfaces and related stainless steel-plastic hybrids. *Appl Surf Sci* 257:9335–9346. doi:10.1016/j.apsusc.2011.05.058
- Petrie EM (2007) Primers and adhesion promoters. In: *Handbook of adhesives and sealants*. McGraw-Hill, New York, pp 277–305
- Malfatti CF, Menezes TL, Radtke C et al (2012) The influence of cerium ion concentrations on the characteristics of hybrid films obtained on AA2024-T3 aluminum alloy. *Mater Corros* 63:819–827. doi:10.1002/maco.201106070
- Kozhukharov S, Kozhukharov V, Schem M et al (2012) Protective ability of hybrid nano-composite coatings with cerium sulphate as inhibitor against corrosion of AA2024 aluminium alloy. *Prog Org Coat* 73:95–103. doi:10.1016/j.porgcoat.2011.09.005
- Hansal WEG, Hansal S, Pölzler M et al (2006) Investigation of polysiloxane coatings as corrosion inhibitors of zinc surfaces. *Surf Coat Technol* 200:3056–3063. doi:10.1016/j.surfcoat.2005.01.049
- Merlatti C, Perrin FX, Aragon E, Margailan A (2008) Evaluation of physico-chemical changes in sub-layers of multi-layer anti-corrosive marine paint systems: plasticizer and solvent release. *Prog Org Coat* 61:53–62. doi:10.1016/j.porgcoat.2007.09.001

21. Yeh J-M, Weng C-J, Liao W-J, Mau Y-W (2006) Anticorrosively enhanced PMMA–SiO₂ hybrid coatings prepared from the sol-gel approach with MSMA as the coupling agent. *Surf Coat Technol* 201:1788–1795. doi:[10.1016/j.surfcoat.2006.03.011](https://doi.org/10.1016/j.surfcoat.2006.03.011)
22. van Ooij WJ (1999) Improved service life of coated metals by engineering the polymer-metal interface. Service life prediction of organic coatings. American Chemical Society, pp 354–377
23. Kim SK, Park IJ, Lee DY, Kim JG (2013) Influence of surface roughness on the electrochemical behavior of carbon steel. *J Appl Electrochem* 43:507–514. doi:[10.1007/s10800-013-0534-5](https://doi.org/10.1007/s10800-013-0534-5)
24. Bastos AC, Ferreira MGS, Simões AMP (2013) Effects of mechanical forming on the corrosion of electrogalvanized steel. *Corros Sci* 69:87–96. doi:[10.1016/j.corsci.2012.11.026](https://doi.org/10.1016/j.corsci.2012.11.026)
25. Orazem ME (2008) Electrochemical impedance spectroscopy. Wiley, Hoboken
26. Eivaz Mohammadloo H, Sarabi AA (2012) The effect of solution temperature and pH on corrosion performance and morphology of nanoceramic-based conversion thin film. *Mater Corros* 64:535–543. doi:[10.1002/maco.201106384](https://doi.org/10.1002/maco.201106384)
27. Plieth W (2008) Electrochemistry for materials science, 1st edn. Elsevier, Amsterdam
28. Suegama PH, Sarmento VHV, Montemor MF et al (2010) Effect of cerium(IV) ions on the anticorrosion properties of siloxane-poly(methyl methacrylate) based film applied on tin coated steel. *Electrochim Acta* 55:5100–5109. doi:[10.1016/j.electacta.2010.04.002](https://doi.org/10.1016/j.electacta.2010.04.002)
29. Zandi Zand R, Verbeken K, Adriaens A (2013) Evaluation of the corrosion inhibition performance of silane coatings filled with cerium salt-activated nanoparticles on hot-dip galvanized steel substrates. *Int J Electrochem Sci* 8:4927–4940
30. Zandi Zand R, Verbeken K, Adriaens A (2013) Influence of the cerium concentration on the corrosion performance of Ce-doped silica hybrid coatings on hot dip galvanized steel substrates. *Int J Electrochem Sci* 8:548–563
31. Garcia-Heras M, Jimenez-Morales A, Casal B et al (2004) Preparation and electrochemical study of cerium-silica sol-gel thin films. *J Alloy Compd* 380:219–224. doi:[10.1016/j.jallcom.2004.03.047](https://doi.org/10.1016/j.jallcom.2004.03.047)
32. Galio AF, Lamaka SV, Zheludkevich ML et al (2010) Inhibitor-doped sol-gel coatings for corrosion protection of magnesium alloy AZ31. *Surf Coat Technol* 204:1479–1486. doi:[10.1016/j.surfcoat.2009.09.067](https://doi.org/10.1016/j.surfcoat.2009.09.067)
33. Zandi Zand R, Verbeken K, Adriaens A (2012) Electrochemical assessment of the self-healing properties of cerium doped sol-gel coatings on 304L stainless steel substrates. *Int J Electrochem Sci* 7:9592–9608
34. Palomino LEM, Suegama PH, Aoki IV et al (2007) Investigation of the corrosion behaviour of a bilayer cerium-silane pre-treatment on Al 2024-T3 in 0.1 M NaCl. *Electrochim Acta* 52:7496–7505. doi:[10.1016/j.electacta.2007.03.002](https://doi.org/10.1016/j.electacta.2007.03.002)
35. Montemor MF, Pinto R, Ferreira MGS (2009) Chemical composition and corrosion protection of silane films modified with CeO₂ nanoparticles. *Electrochim Acta* 54:5179–5189. doi:[10.1016/j.electacta.2009.01.053](https://doi.org/10.1016/j.electacta.2009.01.053)
36. Schem M, Schmidt T, Gerwahn J et al (2009) CeO₂-filled sol-gel coatings for corrosion protection of AA2024-T3 aluminium alloy. *Corros Sci* 51:2304–2315. doi:[10.1016/j.corsci.2009.06.007](https://doi.org/10.1016/j.corsci.2009.06.007)
37. Simões AM, Fernandes JCS (2010) Studying phosphate corrosion inhibition at the cut edge of coil coated galvanized steel using the SVET and EIS. *Prog Org Coat* 69:219–224. doi:[10.1016/j.porgcoat.2010.04.022](https://doi.org/10.1016/j.porgcoat.2010.04.022)
38. Ogle K, Morel S, Jacquet D (2006) Observation of self-healing functions on the cut edge of galvanized steel using SVET and pH microscopy. *J Electrochem Soc* 153:B1–B5. doi:[10.1149/1.2126577](https://doi.org/10.1149/1.2126577)